

## On the Influence of Crystallographic Texture on Pitting Corrosion in Pipeline Steels

V. Venegas<sup>1</sup>, F. Caleyó<sup>1</sup>, L. E. Vázquez<sup>1</sup>, T. Baudin<sup>2</sup>, J. M. Hallen<sup>1</sup>

<sup>1</sup> Departamento de Ingeniería Metalúrgica, IPN-ESIQIE, UPALM, Edif. 7, Zacatenco, México DF 07738, México.

<sup>2</sup> Laboratoire de Physico-Chimie de l'Etat Solide, ICMMO, UMR CNRS 8182, Bâtiment 410, Université de Paris Sud, 91405 Orsay Cedex, France.

\*E-mail: [victoriavenegasreyes@gmail.com](mailto:victoriavenegasreyes@gmail.com)

Received: 16 January 2015 / Accepted: 8 February 2015 / Published: 24 February 2015

---

The influence of crystallographic texture on pitting corrosion is investigated in an API 5L X52 pipeline steel through crystallographic texture and electrochemical studies. Test samples of the studied steel were obtained with similar microstructure and different texture by means of different thermomechanical processes. The texture was characterized by means of X-ray pole figure measurements. The texture-dependent resistance of each sample to pitting corrosion was predicted using a function and an index which combine the susceptibility of crystallographic planes to anodic dissolution and their relative abundance at the material surface, this latter determined by the volume fraction of each texture fiber in the steel. The actual susceptibility of each sample to pitting corrosion was determined by means of cyclic potentiodynamic polarization measurements in two solutions emulating pipeline corrosion environments. The pitting susceptibility predicted from the texture measurements was in good agreement with the susceptibility determined from the cyclic polarization tests. Although the anisotropic nature of anodic dissolution of iron has been known for decades, the use of the crystallographic texture to predict the pitting resistance of pipeline steels conveys a statistical significance not reported until now.

---

**Keywords:** Pitting corrosion, pipeline steels, cyclic polarization, crystallographic texture.

### 1. INTRODUCTION

Although pitting corrosion damage of low-carbon steels has been extensively studied [1, 2], the influence of crystallographic texture in this process have not been fully considered yet. It is well known that in order to avoid or minimize corrosion, the knowledge of the propensity of the material to corrosion is crucial. In this regard, the determination and interpretation of pitting and repassivation

potentials, which measure the tendency of different metal and alloys to pitting, continue to be the main goal of many pitting corrosion studies [1]. The measurement and interpretation of these potentials are not straightforward and have associated many experimental challenges [3, 4]. For example, it is possible to find differences among potential values at different spots of the sample surface because of metallurgical factors such as differences in chemical composition, microstructure, and degree of surface damage [3]. It is also well known that the determination of pitting potential in many materials has associated an uncertainty that can reach hundreds of millivolts, making this kind of potential measurement unsuitable to achieve a fundamental understanding of pitting corrosion [4].

The dependence of anodic dissolution on grain orientation in iron and its alloys has been previously reported by many authors [5–17]. Recently, the anisotropic character of pitting corrosion has been corroborated by mean of microtexture studies based on electron backscatter diffraction (EBSD) together with orientation imaging microscopy (OIM) [18] in polycrystalline iron [13–16]. Scheiber *et al.* [14] established that, during electropolishing, chemical polishing, and electrochemical machining of polycrystalline BCC iron, crystallographic orientation influences anodic dissolution by determining which crystallographic plane becomes the exposed surface at each grain. According to these authors, the dissolution rate of iron during electropolishing or chemical decreases in the sequence  $\{200\} > \{110\} \approx \{222\}$ , while during electrochemical machining this rate increases in the order  $\{200\} < \{110\} < \{111\}$ . Fushimi *et al.* [16] have also used EBSD/OIM to study the anisotropic corrosion of pure BCC iron in sulphuric acid (pH 1). They found that the order of corrosion activity of the  $\{hkl\}$  planes emerging at the material surface was in the order  $\{200\} > \{222\} > \{110\}$  and explained this result on the basis of the decomposed d-valence charge at the material surface.

The dependence of pitting resistance on crystallographic orientation of a 316LVM stainless steel in oxygen-free 1M NaCl aqueous solution was reported by Sahryaria *et al.* [15]. Based on EBSD/OIM studies, these authors found evidence of the anisotropic nature of pitting corrosion and corroborated that the susceptibility of individual grains is strongly dependent on the crystallographic plane emerging at the sample surface. For this material, as measured by the number of pits per grain, the planar orientations  $\{222\}$  and  $\{200\}$  have the highest resistance to pitting corrosion due to the fact that they have the highest point (planar) density in the FCC lattice. This result was in agreement with Kruger's [7] who reported that the number of observed pits on the  $\{110\}$ ,  $\{200\}$ , and  $\{222\}$  crystallographic planes of pure FCC iron decreases in distilled water following this same sequence. Similarly, with the aid of different electrochemical methods, together with EBSD/OIM, Zamanzade and Barnoush [17] found that grains with  $\{110\}$  planes parallel to the surface of Fe<sub>3</sub>Al intermetallics with DO<sub>3</sub> structure show the highest pit density when they corrode in solutions with different concentrations of Cl<sup>-</sup> ions.

In this work a new approach to predict the susceptibility to pitting corrosion of low-carbon pipeline steels is proposed which combines the well-known anisotropic nature of anodic dissolution in BCC iron (ferrite) grains with the role that crystallographic texture plays, as a weight function, in the determination of average physical properties in polycrystalline materials [19]. A texture-related resistance function ( $R_{Tex}$ ) is proposed based on the expected resistance,  $R_{\{hkl\}}$ , of the  $\{hkl\}$  planes emerging at the material surface and the volume fraction,  $V_{TC-\{hkl\}}$ , of the texture components and/or

fibers that determine the relative proportion of these planes in each sample surface according to the crystallographic texture of the sample. This function is given by:

$$R_{Tex} = \left( \sum_{All\ TC-\{hkl\}} V_{TC-\{hkl\}} R_{\{hkl\}} \right) + V_R R_R \quad (1)$$

where  $V_R$  and  $R_R$  refer, respectively, to the volume fraction and pitting resistance of the random texture component, which contains the true random or *phon* texture [18, 19] and orientations not considered explicitly in the parenthesis-enclosed part of  $R_{Tex}$ .

For the estimation of  $R_{Tex}$  in pipeline steels only the typical rolling/recrystallization  $\{hkl\}ND$ <sup>1</sup> texture fibers of BCC steels are needed to be considered [20]; therefore,  $TC-\{hkl\}$  can be replaced by  $\{hkl\}ND$ . Based on the expected resistance of each texture fiber to anodic dissolution, a simpler pitting resistance index ( $I_{Tex}$ ) is also proposed as the ratio of the volume fraction of the high resistance or beneficial ( $V_B$ ) texture fibers to the volume fraction of the low-resistance or detrimental ( $V_D$ ) fibers:

$$I_{Tex} = \frac{V_B}{V_D} \quad (2)$$

It was possible to correlate the value of  $R_{Tex}$  and  $I_{Tex}$  in the studied samples with their actual susceptibility to pitting corrosion as measured by cyclic potentiodynamic polarization (CPP) tests conducted in two different corrosive environments emulating pipeline corrosion conditions. This indicates that the resistance of pipeline steels to pitting corrosion can be foreseen from the knowledge of their crystallographic texture. The results of this study are encouraging because they suggest the possibility of improving the resistance of these steels to pitting corrosion through the control of their crystallographic texture.

## 2. EXPERIMENTAL

A section of a new, 610-mm (24-inch) diameter API 5L grade X52 pipe was used to produce square bars oriented along the rolling direction (RD) of the pipe. These strips were 1.27-cm thick (ND), 1.5-cm wide (transverse direction, TD), and 25-cm long (RD). They served the purpose of having identical starting samples of this API steel, whose chemical composition is shown in Table 1. From this starting material, two groups of test samples (SG1 and SG2) were obtained following different thermomechanical treatments as outlined in Table 2 and described in detail elsewhere [21]. The purpose of these treatments was to obtain samples with similar microstructures but significantly different crystallographic textures.

**Table 1.** Chemical composition (wt%) of the starting API 5L grade X52 steel from which both groups of samples were obtained.

| C     | Mn    | S     | P     | Si    | Cu    | Cr    | Fe      |
|-------|-------|-------|-------|-------|-------|-------|---------|
| 0.212 | 1.334 | 0.032 | 0.028 | 0.037 | 0.021 | 0.009 | Balance |

<sup>1</sup> A fiber of the type  $\{hkl\}ND$  describe the ensemble of orientations for which  $\{hkl\}$  are parallel to the sample rolling plane, so that they are perpendicular to the sample normal direction (ND) [20].

After mechanical grinding/polishing to a 1- $\mu\text{m}$  finish, followed by electropolishing for 2 minutes in a 90% ethanol-10% perchloric acid mixture at  $-70^\circ\text{C}$  and 13V, the texture of the studied samples was quantitatively determined by X-ray diffraction using a Co texture goniometer. Three incomplete pole figures: {110}, {200}, and {111} were measured over a  $1\text{ cm}^2$  on the rolling (RD-TD) plane at mid section of each sample. The experimental pole figures were analyzed using the ADC method [22] in order to obtain the orientation distribution function (ODF) of each sample and the volume fraction of the different texture components and fibers that characterize its texture. The obtained ODFs were computed assuming orthorhombic sample symmetry and represented using Bunge's Euler angles in the cubic-triclinic  $\varphi_2 = 45^\circ$  section of Euler space [19]. Scanning Electron Microscopy (SEM) was used to evaluate the microstructure of each sample after etching in 2% Nital at room temperature for 5 seconds. The average ferrite grain size was estimated in each sample by using the linear intercept method.

**Table 2.** Thermomechanical process followed by each sample group and resulting microstructural features.

| Sample | Reduction (%) | Path              | Rolling Temp. ( $^\circ\text{C}$ ) | Grain Size ( $\mu\text{m}$ ) | Pearlite content (%) |
|--------|---------------|-------------------|------------------------------------|------------------------------|----------------------|
| SG1    | 75            | 2 steps, 50% each | 1040                               | 9                            | 10                   |
| SG2    | 50            | 15 step, 5% each  | 1000                               | 11                           | 14                   |

Cyclic potentiodynamic polarization (CPP) measurements were performed at room temperature using a EG&G-PAR Potentiostat/Galvanostat Model 263A, with a Lock-in Amplifier Model 5210, and a conventional three-electrode cell with a graphite counter-electrode and a saturated calomel electrode (SCE) as reference electrode. A working electrode was prepared for each sample group described in Table 2 with an exposed area of  $0.5\text{ cm}^2$  and embedded in a cylindrical Teflon holder. The samples were wet-ground using SiC paper with grit from 600 up to 4000. They were then polished with an  $\text{Al}_2\text{O}_3$  slurry to obtain a mirror surface. Finally, the working electrode was ultrasonically cleaned (30 s) in methanol and hot-air dried.

Two different solutions were used to carry out the CPP experiments (Table 3). These solutions were selected because they describe well-known typical pipeline corrosion environments [23, 24, 25]. Cyclic polarization was performed after stabilizing the working electrode at open-circuit potential for one hour, starting from  $-1200\text{ mV}$  to a return potential of  $500\text{ mV}$  and back to  $-1200\text{ mV}$  (all vs. SCE), at a scan rate of  $0.16\text{ mVs}^{-1}$ . The area under the observed positive hysteresis loop in each obtained CPP curve was determined for the region from the onset of pitting at the pitting potential ( $E_p$ ) during the positive scan, up to the return potential, and back to the repassivation potential ( $E_R$ ) during the negative scan cycle.

**Table 3.** Chemical composition of the solutions used to conduct the cyclic polarization tests.

| Solution | pH               | $\text{NaHCO}_3$ (M) | $\text{Na}_2\text{SO}_4$ (M) | $\text{NaCl}$ (M) | $\text{Na}_2\text{CO}_3$ (M) |
|----------|------------------|----------------------|------------------------------|-------------------|------------------------------|
| S1       | 9.5 <sup>a</sup> | 0.050                | 0.050                        | 0.050             | 0.025                        |

|    |                  |       |       |       |   |
|----|------------------|-------|-------|-------|---|
| S2 | 6.1 <sup>b</sup> | 0.003 | 0.001 | 0.001 | — |
|----|------------------|-------|-------|-------|---|

<sup>a</sup> Adjusted using NaOH. <sup>b</sup> Adjusted using NHO<sub>3</sub>.

Based on the suitability of the extent of (positive) hysteresis to characterize the susceptibility of a material to pitting corrosion [4], this area was used in this study as a quantitative indicator of the actual susceptibility to pitting corrosion of each sample. It was later compared with the values of  $R_{Tex}$  and  $I_{Tex}$ , predicted from the crystallographic texture measurements, in order to check the capability of these two predictors to forecast the susceptibility of the material to pitting. In the case of solution S1 (Table 3), the crystallographic texture of the samples was determined before and after the CPP test. In each group, the same sample was used to first conduct the X-ray texture measurements, then to carry out the CPP experiments, and finally to perform texture measurements again. In this way it was possible to evaluate the degree of variation in the volume fraction of each considered texture fibers during CPP and so the degree of resistance of each individual fiber to pitting.

### 3. RESULTS

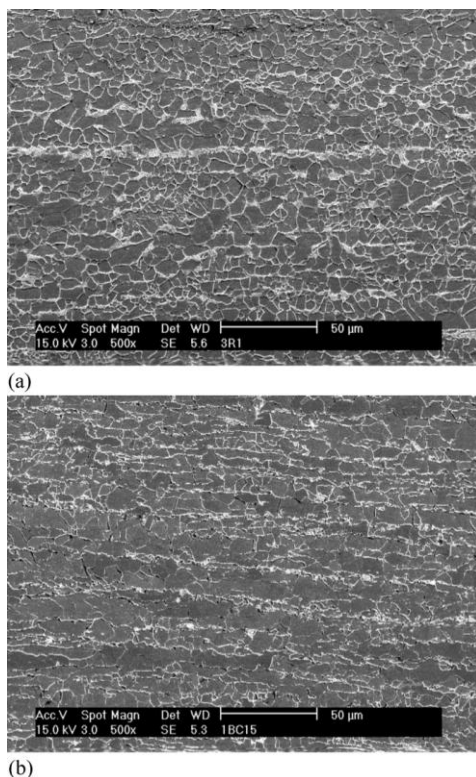


**Figure 1.** Typical SEM micrographs of the studied sample groups. (a) SG1. (b) SG2. In both micrographs the rolling and transverse directions run horizontally and vertically, respectively.

Typical cross-sectional (RD-ND) SEM micrographs of the two studied groups of samples are shown in Fig. 1. The characteristic banded pearlite/ferrite microstructure of low-carbon steels after rolling and recrystallization [20] is observed in both groups. The average grain size and pearlite

content of the two groups of samples was found to be similar as Table 2 shows. The results given in this table and Fig. 1 corroborate that the goal of obtaining test samples with similar microstructures was achieved by the employed thermomechanical treatments outlined in Table 2. This is critical to the present study because this means that the differences behavior respect to the observed pitting corrosion behavior in these samples can be attributed, in a first order approximation, only to the differences in their crystallographic texture.

Figure 2 shows the cubic-orthorhombic representation of the X-ray-derived ODF of the studied samples in the  $\varphi_2 = 45$  deg. section of Euler space before cyclic polarization. The crystallographic texture in the two groups of samples is clearly different and far from the texture of a random polycrystalline sample. However, despite the differences revealed by the and ODFs in Fig. 2, it is noticeable that in both types of samples the texture is characterized by the presence of the  $\{222\}$ ND,  $\{200\}$ ND,  $\{112\}$ ND, and  $\{110\}$ ND texture fibers; yet with significantly different strength between them in each sample and from one sample to the other.

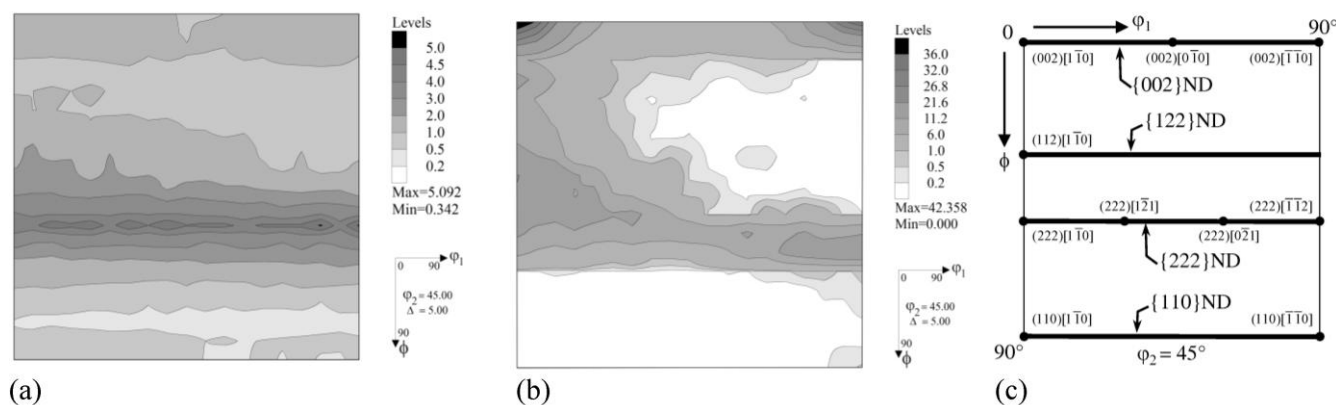


**Figure 2.** X-ray-derived cubic-orthorhombic ODFs of the studied samples before CPP. (a) GS1. (b) GS2. (c) Identification of the texture fibers of interest (in thick lines) in the  $\varphi_2 = 45$  deg. section of Euler space used to represent these ODFs.

Quantitatively, the difference in the volume fraction of each fiber from one sample to another can be used to establish the difference in the value of their  $R_{Tex}$  function and  $I_{Tex}$  index through the observed variations in the  $V_{\{hkl\}}$  values in each fiber and sample. The volume fraction of each one of these four texture fibers, and that of the random part of the texture ( $V_R$ ), was determined in each sample before electrochemically-induced pitting process in solution S1 through the ODF-integration function in the LaboText Software [25] with a 15-deg. dispersion around each ideal  $\{hkl\}$ ND fiber. The results of this process are shown in Table 4.

**Table 4.** Volume fraction of the texture fibers of interest in the tested samples before (B) and after (A) CPP in solution S1.

| Sample | $V_{\{110\}ND}$ |   |                | $V_{\{200\}ND}$ |   |              | $V_{\{112\}ND}$ |   |              | $V_{\{222\}ND}$ |   |              | $V_R$ |   |              |
|--------|-----------------|---|----------------|-----------------|---|--------------|-----------------|---|--------------|-----------------|---|--------------|-------|---|--------------|
|        | B               | A | $\Delta^a(\%)$ | B               | A | $\Delta(\%)$ | B               | A | $\Delta(\%)$ | B               | A | $\Delta(\%)$ | B     | A | $\Delta(\%)$ |

|         |    |    |      |    |    |     |    |    |                 |    |    |     |    |    |                  |
|---------|----|----|------|----|----|-----|----|----|-----------------|----|----|-----|----|----|------------------|
| SG1     | 11 | 17 | +54  | 12 | 12 | 0   | 30 | 32 | +7 <sup>b</sup> | 23 | 13 | -44 | 24 | 27 | +12 <sup>b</sup> |
| SG2     | 3  | 6  | +100 | 34 | 47 | +38 | 23 | 14 | -39             | 32 | 28 | -12 | 8  | 5  | -37              |
| Average |    |    | +77  |    |    | +16 |    |    | -16             |    |    | -28 |    |    | -12              |

<sup>a</sup> Relative to the initial (before CPP) value. <sup>b</sup> Did not behave as expected.

In order to compute the value of  $R_{Tex}$  for each test sample, the texture fibers considered in Table 4 were used in expression (1); this lead to a simplified version of this expression:

$$R_{Tex} = V_{\{110\}ND}R_{\{110\}ND} + V_{\{200\}ND}R_{\{200\}ND} + V_{\{112\}ND}R_{\{112\}ND} + V_{\{222\}ND}R_{\{222\}ND} + V_R R_R \quad (3)$$

The resistance of each fiber  $\{hkl\}ND$  to anodic dissolution  $R_{\{hkl\}}$  was estimated based on the point density ( $\rho_{\{hkl\}}$ , in number of points per area unit) associated with the crystallographic plane  $\{hkl\}$  which lies parallel to the RD-TD plane (perpendicular to ND) of the sample at its surface. In a BCC lattice  $\rho_{\{hkl\}}$  can be calculated as:

$$\rho_{\{hkl\}} = \frac{2}{a_0^2 \sqrt{(h^2 + k^2 + l^2)}} \quad (4)$$

where  $a_0$  refers to the lattice parameter, which is 2.866 Å for pure BCC iron.

The indices  $h$ ,  $k$ , and  $l$  in Eq. (4) must be used with extreme caution, always considering systematic extinctions due to cell centering [27, 28]. In the case of a BCC lattice, they must satisfy the condition that  $h + k + l = 2n$ , that is, an even number.

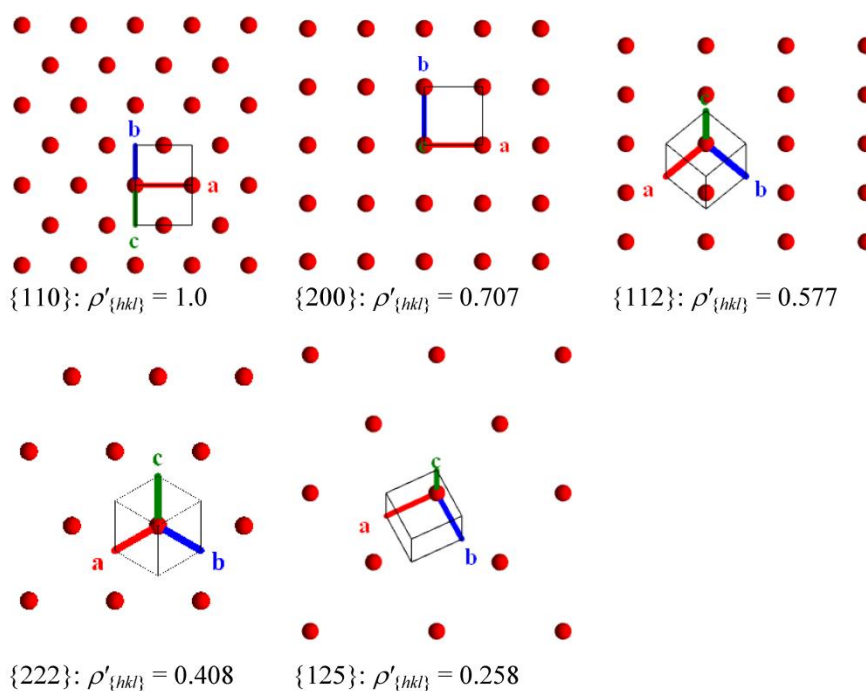


**Figure 3.** Point distribution for some crystallographic planes in a BCC lattice. The numerical value of the point density of each plane is given relative ( $\rho'_{\{hkl\}}$ ) to that of the densest packed ( $\{200\}$ ) plane in this lattice.

For example, if {100} is used instead of {200}, one would arrive to the wrong conclusion that the highest point density occurs for the {001} planes (and not for the {110}) because  $h^2 + k^2 + l^2$  will have the lowest possible value so that  $\rho_{\{100\}}/\rho_{\{hkl\}} > 1$ . If the {200} indices are used instead, one correctly obtains that  $\rho_{\{200\}}/\rho_{\{110\}} < 1$  and  $\rho_{\{110\}}/\rho_{\{hkl\}} > 1$ . This agrees with the well-known fact that the {110} planes have the highest point density in a BCC lattice [28]. Figure 3 shows how  $\rho_{\{hkl\}}$  reduces with  $h^2 + k^2 + l^2$ . This figure illustrates the also fact that point density drastically decreases for crystallographic planes with high Miller indices. If this reduction in point density is translated an increase in the dissolution rate as has been postulated in previous works [7, 14, 15], then it is reasonable to postulated that {hkl} planes with low Miller indices will show a higher resistance to anodic dissolution. The development of crystallographic corrosion pits (corrosion figures) constitutes a good example of orientation-dependent dissolution rate [2, 17].

Based on the above discussion, the resistance of each {hkl}ND fiber to anodic dissolution was defined as the ratio of the point density of the {hkl} plane ( $\rho_{\{hkl\}}$ ) to that of the densest packed plane in the BCC lattice ( $\rho_{\{200\}}$ ), under the constraint  $h^2 + k^2 + l^2 = 2n$ :

$$R_{\{hkl\}ND} = \frac{\rho_{\{hkl\}}}{\rho_{\{200\}}} = \frac{\sqrt{2}}{\sqrt{h^2 + k^2 + l^2}}; \quad h+k+l=2n \tag{5}$$

Figure 4 shows how  $R_{\{hkl\}ND}$  behaves with  $h^2 + k^2 + l^2$ , for  $h, k$ , and  $l \leq 8$ . This function decreases rapidly as the Miller indices of the crystallographic planes increase and then attains a relatively constant value for  $h^2 + k^2 + l^2 > 20$ . The average value of  $R_{\{hkl\}ND}$  in the interval  $20 < h^2 + k^2 + l^2 < 164$ ,  $\langle R_{\{hkl\}ND} \rangle = 0.18$ , was taken as the resistance to pitting corrosion of the random component of the material, that is,  $R_R = 0.18$ .

Based on the numerical values obtained for  $R_{\{hkl\}ND}$  under this approach, the texture-dependent pitting resistance index  $I_{Tex}$  was computed on the assumption that the high-resistance fibers are those for which  $R_{\{hkl\}ND} > 0.5$ , while the low-resistance fibers are those for which such a condition does not hold. This leads to an expression for  $I_{Tex}$  of the type:

$$I_{Tex} = (V_{\{110\}ND} + V_{\{200\}ND}) / (V_{\{112\}ND} + V_{\{222\}ND} + V_R) \tag{6}$$

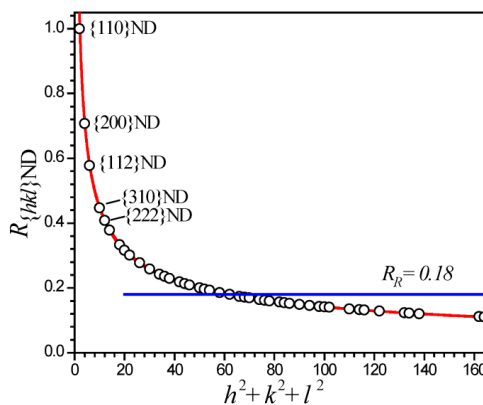
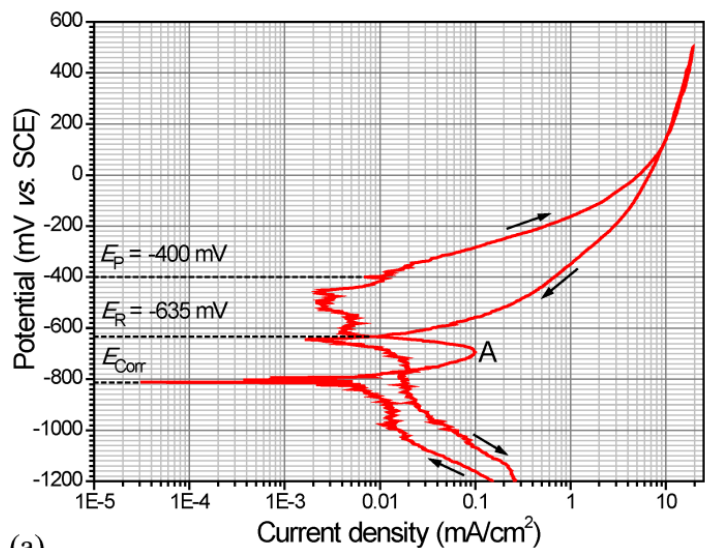
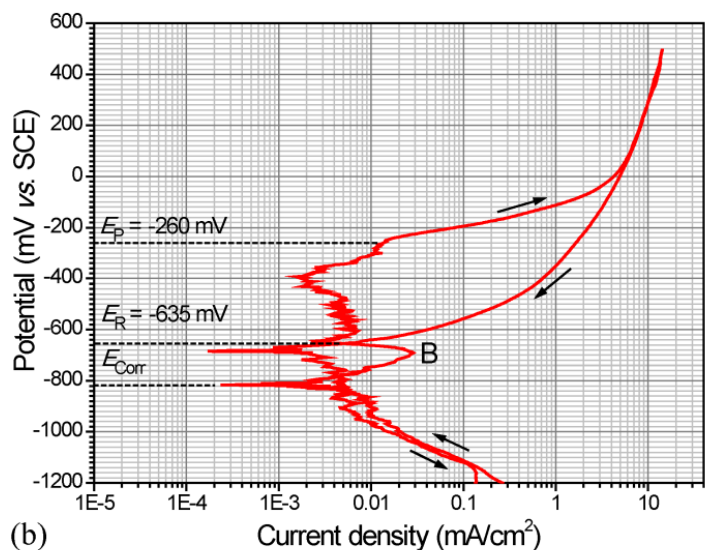


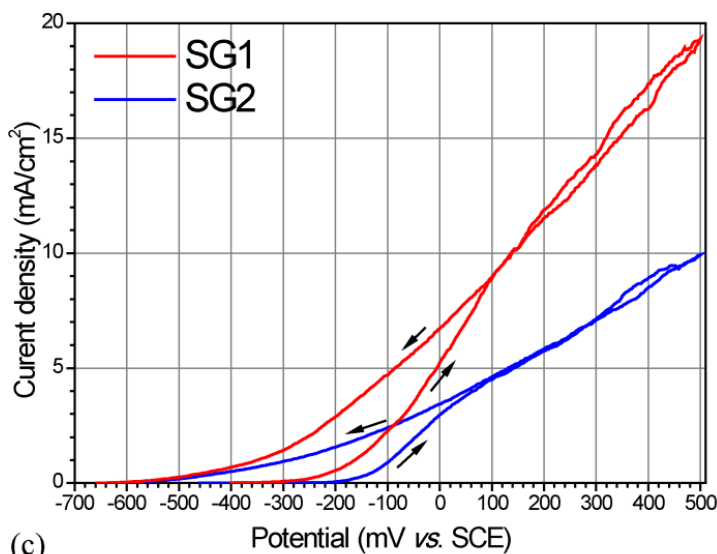
**Figure 4.** Values of  $R_{\{hkl\}ND} = \rho_{\{hkl\}}/\rho_{\{110\}}$  as a function of  $h^2 + k^2 + l^2$ . The value of  $R_R$  was equated to the average value of  $R_{\{hkl\}ND}$  for  $h^2 + k^2 + l^2 > 12$  (blue line). The points and red line represent, respectively,  $R_{\{hkl\}ND}$  values with and without the constraint  $h^2 + k^2 + l^2 = 2n$  in Eq. (5).



(a)



(b)



(c)

**Figure 5.** Experimental CPP curves of the studied samples in solution S1. (a) Group SG1. (b) Group SG2. (c) Positive hysteresis loop in both groups. The arrows indicate the scan direction.

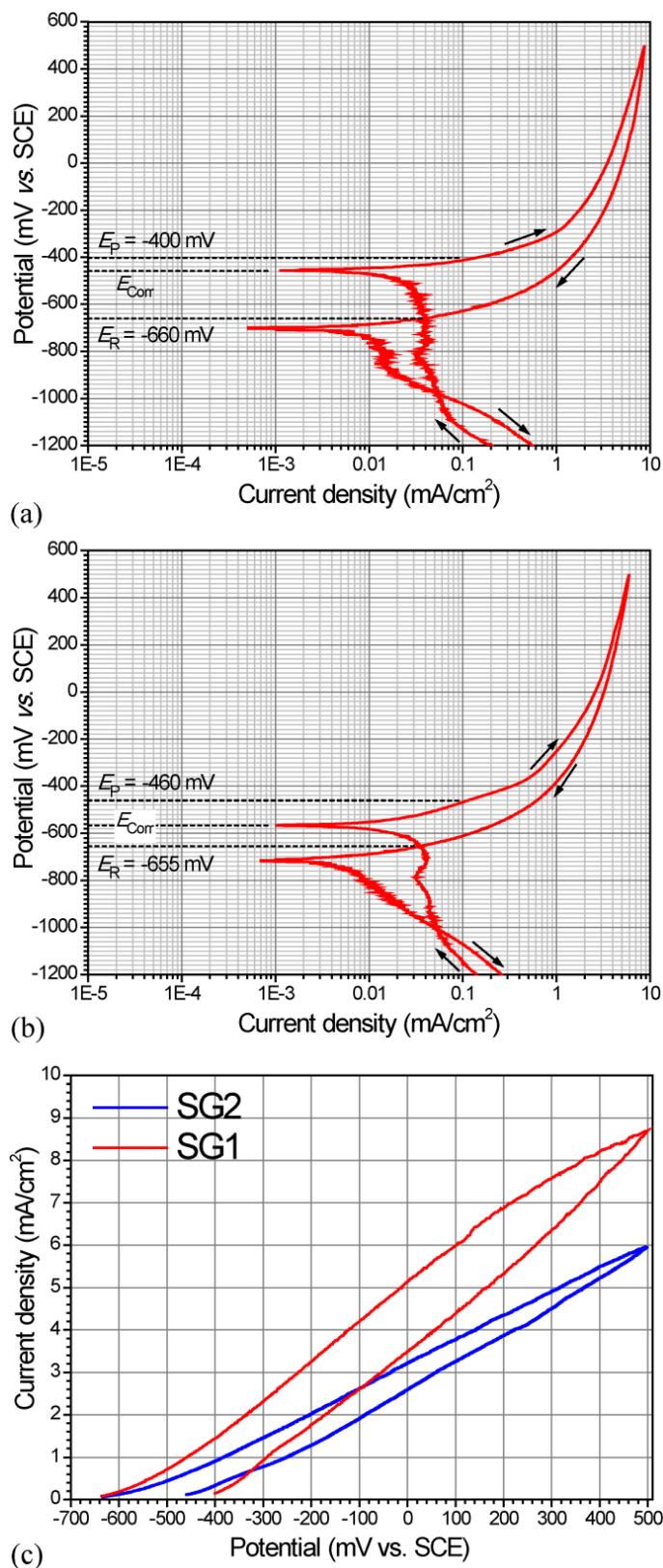


**Figure 6.** Experimental CPP curves of the studied samples in solution S2. (a) Group SG1. (b) Group SG2. (c) Positive hysteresis loop in both groups. The arrows indicate the scan direction.

From the values of  $V_{\{hkl\}ND}$  (Table 4, before CPP) and  $R_{\{hkl\}ND}$  (Eq. (3) and Fig. 5)  $R_{Tex}$  and  $I_{Tex}$  were computed for each test sample using Eqs. (4) and (6), respectively. The results of these computations are shown in Table 5, where some of the information given in Table 4 and Fig. 5 are repeated for the sake of clarity.

**Table 5.** Values of  $V_{\{hkl\}ND}$ ,  $R_{\{hkl\}ND}$ ,  $R_{Tex}$  and  $I_{Tex}$  obtained for the studied samples.e

| Sample | $V_{\{110\}}$ | $R_{\{110\}}$ | $V_{\{200\}}$ | $R_{\{200\}}$ | $V_{\{112\}}$ | $R_{\{112\}}$ | $V_{\{222\}}$ | $R_{\{222\}}$ | $V_R$ | $R_R$ | $R_{Tex}$ | $I_{Tex}$ |
|--------|---------------|---------------|---------------|---------------|---------------|---------------|---------------|---------------|-------|-------|-----------|-----------|
|        | ND            |       |       |           |           |
| SG1    | 11            | 1.000         | 12            | 0.707         | 30            | 0.577         | 23            | 0.408         | 23    | 0.180 | 50        | 0.29      |
| SG2    | 3             |               | 34            |               | 23            |               | 32            |               | 8     |       | 55        | 0.59      |

The results shown in Table 5 indicate that, as measured by their  $R_{Tex}$  and  $I_{Tex}$ , the group SG2 is expected to have a reduced susceptibility to pitting corrosion with respect to group SG1, with the value of  $I_{Tex}$  conveying this information more clearly. To find evidence that supports this prediction the area of the positive hysteresis ( $A_H$ ) part of each obtained CPP curve was computed from the onset of pitting (at  $E_P$  during upward scanning) to repassivation (at  $E_R$  during downward scanning). As mentioned, this area can be interpreted as a direct measure of the extension of pitting undergone by the working electrode during CPP [4].

Figures 5 and 6 show the CPP curves for sample groups SG1 and SG2, respectively, while Table 6 gives the values of  $A_H$ ,  $E_P$ ,  $E_R$ , and  $E_P - E_R$  obtained in each case together with the corresponding values of  $R_{Tex}$  and  $I_{Tex}$ . For the sake of comparison and clarity, Fig. 5c (SG1 and SG2 in S1) and Fig. 6c (SG1 and SG2 in S2) only show the region used to compute  $A_H$ , using a linear scale for the corrosion current.

**Table 6.** Numerical results of the CPP tests compared with the texture-dependent pitting resistance function  $R_{Tex}$  and index  $I_{Tex}$ .

| Solution | Sample | $A_H (\times 10^{-6} \text{ J/cm}^2)$ | $E_P$ (mV) | $E_R$ (mV) | $E_P - E_R$ (mV) | $R_{Tex}$ | $I_{Tex}$ |
|----------|--------|---------------------------------------|------------|------------|------------------|-----------|-----------|
| S1       | SG1    | 483                                   | -400       | -635       | 235              | 50        | 0.29      |
|          | SG2    | 263                                   | -260       | -635       | 375              | 55        | 0.59      |
| S2       | SG1    | 685                                   | -400       | -660       | 260              | 50        | 0.29      |
|          | SG2    | 276                                   | -460       | -655       | 195              | 55        | 0.59      |

Although there are important differences between the electrochemical behavior of both groups of samples in solutions 1 and 2 (for example, a distinguishable passivation process is observed in S1 and not in S2), in both solutions both samples exhibited positive hysteresis during CPP indicating their susceptibility to pitting corrosion. The results presented in Fig. 5 and Table 6 indicate that the extent of positive hysteresis, as measured by  $A_H$ , and therefore the susceptibility to pitting corrosion, is in good agreement with the predictions made from the  $R_{Tex}$  and  $I_{Tex}$  values in both groups of samples in both

solutions. This comes to support the hypothesis made earlier that, from one sample to another, lower values of  $R_{Tex}$  and  $I_{Tex}$  point toward a higher susceptibility to pitting corrosion and viceversa.

#### 4. DISCUSSION

The results presented in Tables 4 to 6 can be used to assess the relationship between crystallographic texture and pitting corrosion in the investigated steels in two different ways. On the one hand, the changes in volume fraction of the different texture fibers that describe the texture of the steel can be related to the relative resistance of each one of them to anodic dissolution.

A statistically significant relative change ( $\geq 10\%$ ) in volume fraction after the CPP test of a given texture fiber can be associated with a poor resistance to pitting corrosion if the change is negative and with a better resistance to this damage if the change is positive. If fibers  $\{110\}ND$  and  $\{200\}ND$  are considered those with better resistance to pitting, as their  $R_{\{hkl\}ND}$  values (Table 5 and Figs. 3 and 4) indicate, then the change in volume fraction in Table 4 should be positive (or remain unchanged) for them if they actually offered a relatively enhanced resistance to pitting during the CPP tests. Conversely, a reduction in volume fraction should be observed for the fibers for which a reduced resistance is expected according to their  $R_{\{hkl\}ND}$  values. These two conditions were fulfilled in most of the cases (8 out of 10) presented in Table 4. This, together with the information given in the last row of this table, corroborate that, in the steel under study, the resistance to pitting corrosion follows the following order  $\{110\}ND; \{200\}ND > \{222\}ND > \{112\}ND > \text{Random}$ . This is in agreement with the studies conducted at microscopic scale [5, 6, 8, 14] but has the novelty that in this study it has been proven at a macroscopic scale, determined by the global crystallographic texture of the studied samples.

On the other hand, Tables 5 and 6 clearly evidence the relationship between the actual pitting resistances, as measured by the value of  $A_H$  obtained in each sample in the two used solutions, and the crystallographic texture-dependent resistance to this damage predicted by the values of  $R_{Tex}$  and  $I_{Tex}$ . In both corrosive solutions, the sample of the SG2 group has associated higher  $R_{Tex}$  and  $I_{Tex}$  values and exhibited a higher resistance to pitting, as their lower  $A_H$  evidenced with respect to the sample in SG1. Although not in the scope of this study, the higher dissolution current observed in SG2 in solution S1 in the active region of the CPP curve before passivation (points A vs. B in Figs. 5a and 6a, respectively) indicate a higher susceptibility to anodic dissolution of this sample not only during pitting, but also for generalized corrosion. It is also important to underline that if the extent of positive hysteresis (and therefore the susceptibility to pitting) is only assessed by the difference between the pitting and repassivation potentials ( $E_P - E_R$ ), then the results might not be (as for samples in SG2, Table 6) so consistent as in the case when  $A_H$  is used to make this assessment.

The information given in Table 4 can be used to explain the results so far discussed. The samples of group SG2 have associated the larger volume fraction (37%) of beneficial (with respect to pitting resistance) texture fibers ( $\{110\}ND$  and  $\{200\}ND$ ), while the samples of SG1 has the smaller proportion (23%) of these fibers. Conversely, these latter samples have associated the largest proportion (79%) of harmful texture fibers ( $\{222\}ND$ ,  $\{112\}ND$  and Random), whereas the proportion

of these fibers in SG2 is 63%. At this point, it is important to stress that the resistance to pitting corrosion of a given sample should not be solely assessed by comparing the relative abundance of high-resistance and low-resistance texture fibers but by computing their ratio as in Eq. (6). For example, this ratio is 0.59 for the sample in SG2 and 0.29 for those in SG1, indicating that the former are as twice as resistant as the latter as the CPP tests corroborate. Accordingly  $I_{Tex}$  helps determine more accurately which sample will show a better resistance to pitting corrosion in the material when one has a good idea of which fibers offer a relatively high resistance to anodic dissolution and which do not. If such knowledge is absent, or the boundary between high- and low-resistance texture fibers is not as clear as in pure BCC iron, then the use of  $R_{Tex}$  would be more appropriate.

All those results confirm the hypothesis of this work that the resistance to pitting corrosion of pipeline steels is significantly influenced by the crystallographic texture of the material because of the anisotropic anodic dissolution of the ferrite phase and the fact that crystallographic texture determines the relative proportion of  $\{hkl\}$  planes emerging at the material surface.

## 5. CONCLUSIONS

The results obtained in this work evidence that the resistance of pipeline steels to pitting corrosion can be foreseen from the knowledge of their crystallographic texture because of two important facts: (i) the anisotropic behavior of anodic dissolution of one of their major constituent (ferrite), and (ii) the role that crystallographic texture plays in determining the average value of physical properties in polycrystalline materials. During pitting corrosion of these steels, the anisotropic dissolution of ferrite is determined by the fact that the resistance to anodic dissolution of a given  $\{hkl\}$  plane family can be correlated to its point (planar) density, as previous works have shown. At the same time, crystallographic texture determines the relative abundance of  $\{hkl\}$  planes at the material surface and thus, the relative abundance of low- and high-resistance planes at the corroding steel surface.

It has been shown that the combined action of these two aspects can be considered through the use of the proposed pitting resistance function  $R_{Tex}$  or, more simply, through the pitting resistance index  $I_{Tex}$ . They can be obtained from the knowledge of the volume fraction of the texture components/fibers in the steels and the relative resistance of each one of them to anodic dissolution. It has been postulated that locally, at a grain scale, this resistance can be estimated from the point density of the  $(hkl)$  plane exposed to the corrosive environment at the steel surface. The resistance of the  $\{hkl\}$ ND texture fibers to pitting corrosion in this studied steel was first assumed and then experimentally observed to decrease in the following order:  $\{110\}$ ND;  $\{200\}$ ND >  $\{222\}$ ND >  $\{112\}$ ND > Random.

The  $R_{Tex}$ - and  $I_{Tex}$ -based pitting-resistance predictions made for the studied pipeline steel were found in good agreement with the results of cyclic potentiodynamic polarization tests. This supports the above mentioned postulate and confirms that the conclusions of previous studies on the anisotropic anodic dissolution of pure iron crystal can be extended, based on the knowledge of their global crystallographic texture, to predict the susceptibility of pipeline steels to pitting corrosion. This shows

a possible path to increase the resistance of these steels to pitting corrosion through the control and/or modification of their crystallographic texture during their fabrication.

#### ACKNOWLEDGEMENTS

One of the authors (L. E. Vázquez) gratefully thanks CIDIM-ESIQIE (project 425101840) of Instituto Politécnico Nacional de México (IPN) for the financial support received during the realization of this work. The comments provided by the reviewers are deeply appreciated.

#### References

1. Z. Szklarska-Smialowska, *Pitting and crevice corrosion*, NACE International, The Corrosion Society, TX, (2005)
2. P. Marcus, *Corrosion Mechanisms in Theory and Practice*, Marcel Dekker Inc., New York, (2002)
3. H. Kaesche, *Corrosion of Metals, Physicochemical Principles and Current Problems*, Springer-Verlag, Berlin, (2003)
4. G. S. Frankel, *J. Electrochem. Soc.*, 145 (1998) 2186
5. W. R. Buck, H. Leidheiser, *J. Electrochem. Soc.*, 104 (1957) 474
6. H.J. Engell, *Arch. Eisenhüttenw.*, 7 (1955) 393
7. J. Kruger, *J. Electrochem. Soc.*, 106 (1959) 736
8. J. Mieluch, M. Smialowski, *Corros Sci.*, 4 (1964) 237
9. G. P. Cammarota, L. Felloni, G. Palombarini, S. S. Traverso, *Corrosion* 26 (1970) 129
10. K. Fushimi, K. Azumi, M. Seo, *ISIJ International*, 39 (1999) 346
11. K. Fushimi, M. Seo, *Electrochim. Acta*, 47 (2001) 121
12. M. Chiba, M. Seo, *J. Electrochem. Soc.*, 150 (2003) B525
13. A. Schreiber, J. W. Schultze, M. M. Lohrengel, F. Kálmán, E. Kálmán, *Electrochim. Acta*, 51 (2006) 2625
14. A. Schreiber, C. Rosenkranz, M. M. Lohrengel, *Electrochim. Acta*, 52 (2007) 7738
15. A. Sahyaria, J. A. Szpunar, S. Omanovic, *Corros. Sci.*, 51 (2009) 677
16. K. Fushimi, K. Miyamoto, H. Konno, *Electrochim. Acta*, 55 (2010) 7322
17. M. Zamanzade, A. Barnoush, *Corros. Sci.*, 78 (2014)
18. V. Randle and O. Engler, *Introduction to Texture Analysis. Macrotecture, Microtexture and Orientation Mapping*, Francis & Taylor, London, (2003)
19. H. J. Bunge, *Texture Analysis in Materials Science-Mathematical Methods*, Butterworth-Heinemann, Oxford, (1983)
20. R. K. Ray, J. J. Jonas, *Int. Mater. Rev.*, 35 (1990) 1
21. V. Venegas, F. Caleyo, T. Baudin, J. H. Espina-Hernández, J. M. Hallen, *Corros. Sci.*, 53 (2011) 4204
22. K. Pawlick, *Phys. Status Sol. B*, B134 (1986) 477
23. J. C. Velazquez, F. Caleyo, A. Valor, J. M. Hallen, *Corrosion*, 65 (2009) 332
24. F. Caleyo, J. C. Velazquez, A. Valor, J. M. Hallen, *Corros. Sci.*, 51 (2009) 1925
25. M. C. Li, Y. F. Cheng, *Electrochim. Acta*, 53 (2008) 2831
26. LaboText 3.0, *Texture Analysis Software for Windows*, LaboSoft S.C., (2005)
27. B. D. Cullity, S. R. Stock, *Elements of X-Ray Diffraction*, 3rd Ed., Prentice Hall, New Jersey, (2001)
28. A. Kiejna, K. F. Wojciechowski, *Metal Surface Electron Physics*, Alden Press, Oxford, (1996)